Catalysis Science & Technology

Accepted Manuscript

ROYAL SOCIETY OF CHEMISTRY

www.rsc.org/catalysis

Graphical Abstract:

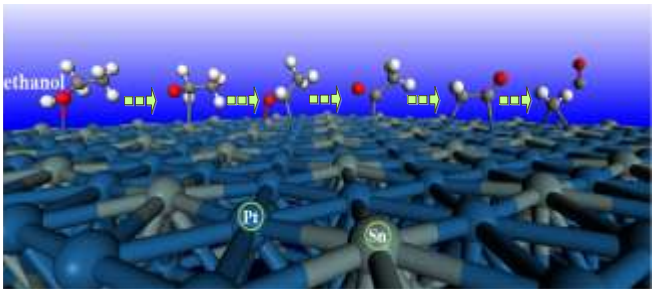

Periodic density functional theory and microkinetic modeling were performed to elucidate the effect of Sn content on the CO tolerance of $Pt_3Sn(111)$ catalyst in ethanol decomposition. Beneficial from the easy-oxidated CH_3CO, hard-forming but readily-desorbed CH_2CO, and the less competitive C–C bond scission, the formation of CO is not facile on $Pt_3Sn(111)$. The Sn content plays "bifunctional" and "ligand effect" roles to effectively strengthen the O-end species adsorptions, adjust the alloy electronic structures, weaken the Pt–CO bonds, and thus facilitating CO elimination from $Pt_3Sn(111)$.

Journal Name

RSCPublishing

ARTICLE

CO tolerance of $Pt_3Sn(111)$ catalyst in ethanol decomposition

Cite this: DOI: 10.1039/x0xx00000x

Xiaoqing Lu,[a*] Zhigang Deng,[a,b] Shuxian Wei,[a] Qing Zhu,[a] Weili Wang,[a] Wenyue Guo[a*] and Chi-Man Lawrence Wu[b,c]

Received 00th January 2015,
Accepted 00th January 2015

DOI: 10.1039/x0xx00000x

www.rsc.org/

CO tolerance is one of the crucial factors to protect catalysts against inactivation along ethanol decomposition processes. Herein, the intrinsic essence of CO tolerance and the effect of alloying element Sn in $Pt_3Sn(111)$ are investigated by combining periodic density functional theory (DFT) and microkinetic modelling. It is found that the most competitive route to CO proceeds via $CH_3CH_2OH \rightarrow CH_3CH_2O \rightarrow CH_3CHO \rightarrow CH_3CO \rightarrow CH_2CO \rightarrow CH_2 + CO$. Beneficial from the easily-oxidated CH_3CO, hard-forming but readily-desorbed CH_2CO, and the less competitive C–C bond scission occurs before the C^{α}–H, C^{β}–H, and O–H bond scission, the formation of CO is not facile on $Pt_3Sn(111)$. The alloying element Sn plays "bifunctional" and "ligand effect" roles to effectively strengthen the O-end species adsorptions, adjusts the alloy electronic structures, weakens the Pt–CO bonds, and thus facilitating CO elimination from $Pt_3Sn(111)$. Microkinetic modelling confirms the substantially high CO tolerance of Pt_3Sn, and easy desorption for the most abundant species of CH_2CO and CH_2 from surface above the room temperature. This theoretical work sheds new light on the CO tolerance of $Pt_3Sn(111)$ in ethanol decomposition, and provides a fresh perspective in understanding the effect of alloying elements.

1. Introduction

Ethanol has attracted wide attention as promising fuel material due to the high energy density, low toxicity, and facile storage and renewability,[1] especially in the applications of direct ethanol fuel cells (DEFCs)[2] and biofuel cells.[3] Decomposition and oxidation of ethanol usually occurs on an efficient catalyst surface,[4-6] but it also causes CO poisoning, thus affecting the consumption efficiency of fuels.[3,7-9] So, one of the key issues to improve catalytic performance is to explore efficient catalysts with outstanding CO tolerance for ethanol conversion. Pt-based alloys have been proposed to alleviate the CO poisoning problem via the addition of alloying elements,[10] such as W,[11] Mo,[11-13] Fe,[14] Co,[15] Ni,[16] Sn,[11,17-20] Rh,[21] Ru[11,22] and Pd[23]. Previous experimental work showed that the enhancement in the activity of bimetallic alloys was mainly through the "bifunctional" and "ligand effects" mechanisms.[22,24] It has been proposed that the bifunctional mechanism is due to the existence of the second atom at the bimetallic alloy surface that affects the adsorption of the O-containing species, and promotes the oxidative removal of CO.[25-27] As for the ligand effect, the added atom changes the electronic structure of Pt and weakens the Pt–CO bond, thereby the surfaces become more active for CO elimination.[15,28,29] Pt_3Sn accounts for the large proportion of PtSn alloy phases and exhibits high catalytic activity in fuel cell.[30-34] Xu *et al.*[35] carried out DFT calculations to study the adsorption and initial dehydrogenation of ethanol on Pt_3M (M = Pt, Ru, Sn, Re, Rh and Pd) clusters, and found that Pt_3Sn was the most active catalyst among all of the alloy metals for the initial oxidation of ethanol, because the Sn atom could enhance the rate constant of dehydrogenation by the α-hydrogen path on the Pt site of Pt_3Sn. Alcala *et al.*[30] found that the Sn atoms on PtSn-based catalysts could facilitate the dehydrogenation of ethanol to acetaldehyde and inhibit the decomposition of ethanol to CO, CH_4 and C_2H_6 using reaction kinetics studies; these experimental observations were further interpreted using DFT calculations on Pt(111) and $Pt_3Sn(111)$, and it was found that the inhibitions was due to the suppression effect on C–C and C–O bond scissions. However, an in-depth theoretical analysis of ethanol decomposition on Pt_3Sn alloy surface has not been reported yet. In particular, questions surrounding the selectivity of adsorption, the sequence of bond activation of different type bonds, the competitive reaction mechanisms, especially for the intrinsic essence of CO tolerance, the crucial effect of alloying element Sn on each elementary process, *etc.*, have not been convincingly elucidated.

To fully solve the puzzles, we present a systematic investigation on ethanol decomposition on $Pt_3Sn(111)$, by elucidating the electronic structure alteration of catalyst, selectivity of adsorption, sequence of bond scission, competition of elementary reaction process, thermodynamic and kinetic properties, coverage of residue, *etc.*, to highlight the intrinsic essence of CO tolerance of $Pt_3Sn(111)$ and the effect of Sn alloying. The adsorption configurations, energies, potential energy surfaces, energy barrier analysis, and intermediate coverage were performed by combining the periodic density functional theory (DFT) and microkinetic modelling, which has been successfully applied to similar systems in our previous studies.[36]

2. Computational details

Periodic DFT calculations were performed with the DMol^3 program package in Materials Studio of Accelrys Inc.[37-39] The exchange-correlation functional of GGA-PW91 approximation was used.[40-42] To take the relativity effect into account, the density functional semicore pseudopotential (DSPP)[43] method was employed for the Pt and Sn atoms, whereas the C, H and O atoms were treated with an all-electron basis set. The valence electron functions were expanded into a set of numerical atomic orbital by a double-numerical basis with polarization functions (DNP). A Fermi smearing of 0.005 Hartree and a real-space cut-off of 4.5 Å were used to improve the computational performance. The $Pt_3Sn(111)$ surfaces were modelled as a p(2 × 2) surface unit cell and four layers slab, with the uppermost two layers relaxed together with the adsorbate, while the remaining two substrate layers were fixed in their bulk positions. A vacuum region of 12 Å was used. The reciprocal space was sampled with a (5 × 5 × 1) *k*-points grid generated automatically using the Monkhorst-Pack method.[44] A single adsorbate was allowed to adsorb on one side of the slab, which corresponds to a molecular coverage of 0.25 ML. The calculated lattice constants for Pt_3Sn is 4.01 Å, which in good agreement with the experimental value of 4.00 Å.[45] We also performed calculations on a four-layer p(4 × 4) unit cell, and the adsorption energy of *trans*-ethanol at T^{Pt} site (top site of Pt) were found to deviate from the value determined on p(4 × 4) cell by less than 0.02 eV, indicating that the coverage effect is not significant for the adsorption.

The adsorption energies (E_{ads}) were calculated using the following equation:

$$E_{ads} = E_{gas} + E_{sub} - E_{gas/sub} \quad (1)$$

where E_{gas}, E_{sub} and $E_{gas/sub}$ are the total energies of the free adsorbate, clean $Pt_3Sn(111)$ slab, and adsorbate on $Pt_3Sn(111)$, respectively. With this definition, a positive E_{ads} implies a stable adsorption.

Transition state (TS) searches were performed at the same theoretical level with the complete Linear Synchronous Transit/Quadratic Synchronous Transit (LST/QST) method implemented in DMol^3.[46] We applied the TS theory formalism to predict rate constants for all the elementary steps involved. The rate constant k and pre-exponential A^0 were estimated using conventional TS theory:[47,48]

$$k = \frac{k_B T}{\hbar}\frac{Q_{TS}}{Q_{IS}}\exp(\frac{-E_a}{RT}) = A^0\exp(\frac{-E_a^0}{RT}) \quad (2)$$

$$Q = \prod_{i=1}^{3N}\frac{e^{-h\nu_i/2k_BT}}{1-e^{-h\nu_i/k_BT}} \quad (3)$$

where k_B is the Boltzmann constant, R is the gas constant, $\hbar$ is the Planck's constant, T is the temperature following experimental conditions for Pt-based catalysts (300 K),[30] E_a^0 and E_a are energy barriers with and without zero point energy (ZPE) corrections. Q_{IS} and Q_{TS} are the partition functions respective at the IS and TS, and ν_i are the frequencies of the vibration modes.

3. Results

In this section, the adsorptions of ethanol and surface species involved are first described. Then, the most facile elementary reaction steps are analysed to gather a general view on the reaction process.

3.1 Adsorption

The possible adsorption sites of $Pt_3Sn(111)$ are labeled by local coordination: (1) two top sites (T^{Pt} and T^{Sn}), (2) two bridge sites (B^{2Pt} and B^{PtSn}), and (3) four hollow sites (H^{2PtSn}, H^{3Pt}, F^{2PtSn} and F^{3Pt}), as shown in Fig. 1. The most stable configuration of each surface intermediate is determined by comparing with all other configurations identified in the searching processes. Table 1 lists the adsorption energies and geometrical parameters of the involved reaction intermediates. The selected configurations of each reaction intermediate along the possible reaction pathways are shown in Fig. 2, and other metastable configurations are provided in Electronic supplementary information (ESI) Fig. S1.

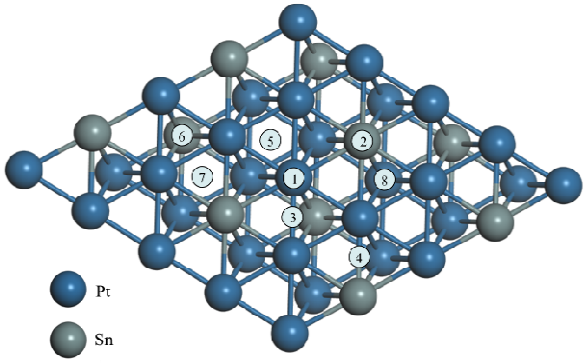

Fig. 1. The high symmetric adsorption site on $Pt_3Sn(111)$; 1: T^{Pt}; 2: T^{Sn}; 3: B^{2Pt}; 4: B^{PtSn}; 5: F^{3Pt}; 6: H^{3Pt}; 7: F^{2PtSn}; 8: H^{2PtSn}. For clarity, a large (4 × 4) unit cell is adopted.

Ethanol (CH_3CH_2OH). For the gas-phase CH_3CH_2OH, two stable iso-energetic isomers of *trans*- and *cis*-conformer are confirmed.[1] For *trans*-ethanol, the bond lengths are calculated to be 0.97 (0.95 Å) for the O–H bond, 1.43 (1.42 Å) for the C–O bond, 1.52 (1.50 Å) for the C–C bond; the C–C–O angle is 108° (108°), and is in good agreement with experimental values (in parentheses).[49] On $Pt_3Sn(111)$, ethanol is found to adsorb weakly at the top site via the O atom, giving two kinds of configurations (η^1(O)-*trans* and η^1(O)-*cis*). At the T^{Sn} site, the η^1(O)-*trans* and η^1(O)-*cis* modes account for the very close binding energy (0.51 and 0.49 eV). Structurally, for adsorbed *trans*-ethanol (see Fig. 2), the C–O axis is tilted 60° from the surface normal; the O–Sn and C–O distances are 2.66 and 1.46 Å. For the *cis*-ethanol adsorption (see Fig. 2), the C–O axis is tilted 65°. The large O–Sn distance (2.71 Å) is in consistent with the weak adsorption of ethanol, which similar to the ethanol adsorbed on Rh(111)[1], Pd(111)[50] and Pt(111).[51] At the T^{Pt} site, the η^1(O)-*trans* and η^1(O)-*cis* modes have the weak adsorptions of 0.40 and 0.31 eV, respectively. As shown in Fig. 2, for the adsorbed *trans*-ethanol at the T^{Pt} site, the C–O axis is tilted 49°; the O–Pt and C–O distances are 2.58 and 1.45 Å, respectively. The *cis*-ethanol involves a larger O–Pt distance of 2.70 Å, which corresponds to the weakest adsorption.

Ethoxide (CH_3CH_2O). T^{Sn} is the most favorable site for CH_3CH_2O adsorption. The adsorption energy is calculated to be 1.81 eV, which is 0.2 eV larger than the adsorption at the T^{Pt} site. Also, the B^{2Pt}, B^{PtSn} and F^{2PtSn} adsorption configurations are stable with the adsorption energies of 1.76, 1.73 and 1.71 eV, respectively. As shown in Fig. 2, the C–O bond is tilted 63° in the most stable configuration of the T^{Sn} adsorption; the C–O and O–Sn bond lengths are 1.42 and 2.06 Å, respectively. For the B^{2Pt} adsorption configuration in Fig. 2, the C–O bond is tilted by 34°, and the two O–Pd bond lengths are around 2.24 Å (see Fig. 2). The B^{PtSn} adsorption configuration involves the C–O bond to be tilted by 44° from the surface normal, and the O–Pt and O–Sn bond lengths are 2.23 and 2.31 Å, respectively (see Fig. S1). For both bridge adsorptions, the C–O bonds are slightly elongated to 1.44 Å. In the case of F^{2PtSn} adsorption, the C–O axis is only tilted by 19°; two O–Pt and one O–Sn bond lengths are 2.27, 2.30 and 2.51 Å, respectively (see Fig. S1).

Table 1 Adsorption sites, adsorption energies (in eV) and structural parameters (in angstrom and degree) for intermediates involved in ethanol decomposition to CO on $Pt_3Sn(111)$.

Species	Site	Mode	E_{ads}	$d_{M\text{-}Pt}$	$d_{C\text{-}C}$	$d_{C\text{-}O}$	Angles[a]
CH_3CH_2OH	T^{Pt}	η^1(O)-*trans*	0.40	2.58	1.51	1.45	49
	T^{Sn}	η^1(O)-*trans*	0.51	2.66	1.51	1.46	60
	T^{Pt}	η^1(O)-*cis*	0.31	2.70	1.52	1.45	39
	T^{Sn}	η^1(O)-*cis*	0.49	2.71	1.52	1.46	65
CH_3CH_2O	T^{Pt}	η^1(O)	1.61	2.06	1.52	1.42	61
	T^{Sn}	η^1(O)	1.81	2.06	1.52	1.42	63
	B^{PtSn}	η^2(O)	1.73	2.23, 2.31	1.51	1.44	44
	B^{2Pt}	η^2(O)	1.76	2.24, 2.24	1.52	1.44	34
	F^{2PtSn}	η^3(O)	1.71	2.27, 2.30, 2.51	1.51	1.44	19
CH_3CHOH	T^{Pt}	$\eta^1(C^{\alpha})$	1.82	2.14	1.51	1.45	
	T^{Sn}	$\eta^1(C^{\alpha})$	1.05	2.39	1.50	1.43	
CH_2CH_2OH	T^{Pt}	$\eta^1(C^{\beta})$	1.92	2.21	1.51	1.42	
	T^{Sn}	$\eta^1(C^{\beta})$	1.45	2.25	1.52	1.39	
	B^{PtSn}	$\eta^1(C^{\beta})$-η^1(O)	1.67	2.12, 2.62	1.51	1.45	75
CH_3CHO	T^{Sn}	η^1(O)-V[b]	0.45	2.46	1.49	1.22	80
	T^{Sn}	η^1(O)-P[b]	0.35	2.86	1.49	1.23	47
CH_2CH_2O	B^{2Pt}	$\eta^1(C^{\beta})$-η^1(O)	0.74	2.07, 2.11	1.52	1.40	65
	B^{PtSn}	$\eta^1(C^{\beta})$-η^1(O)	1.10	2.08, 2.14	1.51	1.41	70
	F^{2PtSn}	$\eta^1(C^{\beta})$-η^2(O)	0.96	2.13, 2.28, 2.28	1.52	1.43	36
	H^{2PtSn}	$\eta^1(C^{\beta})$-η^2(O)	0.82	2.12, 2.26, 2.32	1.53	1.44	37
CH_3CO	T^{Pt}	$\eta^1(C^{\alpha})$	2.26	2.05	1.51	1.21	61
	T^{Sn}	$\eta^1(C^{\alpha})$	1.08	2.39	1.50	1.20	63
CH_2CHO	B^{2Pt}	$\eta^1(C^{\beta})$-η^1(O)	1.83	2.19, 2.35	1.45	1.27	79
	B^{PtSn}	$\eta^1(C^{\beta})$-η^1(O)	1.95	2.17, 2.49	1.45	1.26	69
CH_2CO	B^{2Pt}	$\eta^1(C^{\alpha})$-$\eta^1(C^{\beta})$	0.73	2.07, 2.11	1.49	1.21	
CHCO	B^{2Pt}	$\eta^2(C^{\beta})$	2.20	2.17, 2.19	1.34	1.17	
	F^{2PtSn}	$\eta^1(C^{\alpha})$-$\eta^2(C^{\beta})$	1.77	2.10, 2.12, 2.28	1.44	1.21	
	F^{3Pt}	$\eta^1(C^{\alpha})$-$\eta^2(C^{\beta})$	1.77	2.10, 2.12, 2.14	1.45	1.20	
	H^{3Pt}	$\eta^1(C^{\alpha})$-$\eta^2(C^{\beta})$	2.53	2.10, 2.12, 2.12	1.45	1.20	
CH_2OH	T^{Pt}	η^1(C)	1.94	2.14		0.98	
	T^{Sn}	η^1(C)	0.82	2.26		0.97	
CH_2O	T^{Pt}	η^1(C)	0.16	3.45		1.22	
	T^{Sn}	η^1(O)	0.36	2.78		1.22	
	B^{2Pt}	η^1(C)-η^1(O)	0.37	2.16, 2.16		1.35	
	B^{PtSn}	η^1(C)-η^1(O)	0.37	2.18, 2.26		1.32	
	F^{2PtSn}	η^1(C)-η^2(O)	0.38	2.13, 2.28, 2.43		1.38	
	H^{3Pt}	η^1(C)-η^2(O)	0.24	2.13, 2.29, 2.34		1.38	
CHO	T^{Pt}	η^1(C)	2.28	2.01		1.21	
	T^{Sn}	η^1(C)	0.78	2.36		1.20	
	H^{3Pt}	η^2(C)-η^1(O)	2.09	2.16, 2.17, 2.20		1.29	
CH_3	T^{Pt}	η^1(C)	1.98	2.11			
	T^{Sn}	η^1(C)	1.33	2.22			
CH_2	B^{2Pt}	η^2(C)	3.96	2.10, 2.10			
	B^{PtSn}	η^2(C)	3.04	2.09, 2.22			
CO	T^{Pt}	η^1(C)	1.45	1.89		1.16	
	T^{Sn}	η^1(C)	0.13	3.21		1.14	
	B^{2Pt}	η^2(C)	1.09	2.06, 2.07		1.18	
	F^{3Pt}	η^3(C)	0.77	2.13, 2.13, 2.15		1.19	
	H^{3Pt}	η^3(C)	1.27	2.13, 2.17, 2.17		1.19	
H	T^{Pt}	η^1(H)	2.77	1.58			
	T^{Sn}	η^1(H)	1.50	1.76			
	F^{3Pt}	η^3(H)	2.70	1.83, 1.83, 1.86			
	H^{3Pt}	η^3(H)	2.95	1.90, 1.90, 1.92			

[a] Values are angles between the surface normal and the C–O axis in the corresponding species. [b] V and P represent the C–C axis almost vertical and parallel to the surface.

Acetaldehyde (CH_3CHO). CH_3CHO has been proposed as a crucial intermediate in ethanol decomposition and synthesis.[52,53] CH_3CHO has two stable adsorption configurations at T^{Sn} site with different C–C slant angles. As seen from Fig. 2, the C–C axis is almost vertical to the surface in the most stable η^1(O)-V mode. CH_3CHO binds to the surface via the O atom with the O–Sn distance of 2.46 Å; the C–O and C–C bond lengths are 1.22 and 1.49 Å, respectively. The corresponding energy is 0.45 eV, which is relatively low due to the closed-shell electronic configuration of the adsorbate. For the T^{Sn} adsorption via the η^1(O)-P mode (see Fig. S1), the C–C axis is almost vertical to the surface with the C–C bond length of 1.49 Å. The O–Sn distance and C–O bond length are 2.86 and 1.23 Å, respectively, and the corresponding adsorption energy is only 0.35 eV.

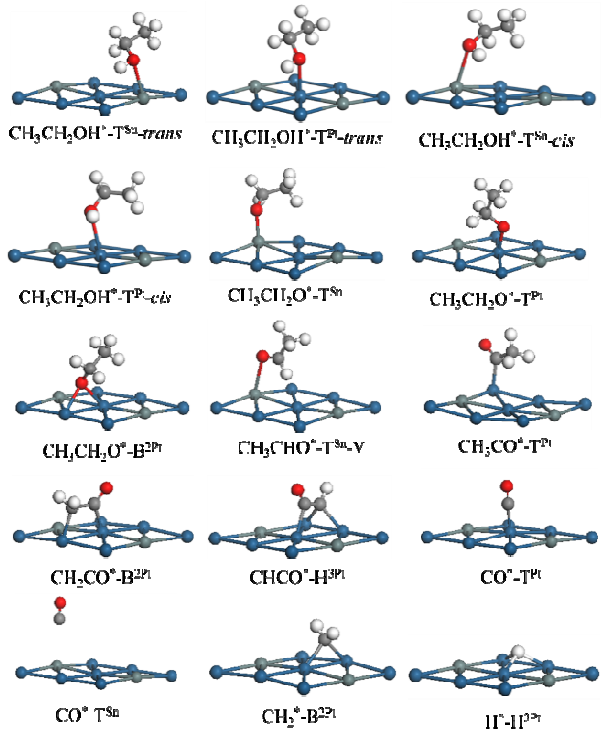

Fig. 2. Configurations of reaction intermediates used to search for reaction pathway of ethanol decomposition to CO on $Pt_3Sn(111)$.

Acetyl (CH_3CO). As shown in Fig. 2, CH_3CO adsorbs stably at the T^{Pt} site via the $\eta^1(C^\alpha)$ mode with a binding energy of 2.26 eV. In this configuration, the C–Pt bond is almost perpendicular to the surface; the C–Pt, C–O and C–C bond lengths are 2.05, 1.21 and 1.51 Å, respectively. These results are similar to our previous studies of CH_3CO adsorbed at the top site on Pd(111).[50] Analogously, CH_3CO can adsorb at the T^{Sn} site with the C–Sn distance of 2.39 Å, and the corresponding adsorption energy is 1.08 eV (see Table 1 and Fig. S1).

Ketene (CH_2CO). CH_2CO is an important intermediate relevant to catalytic C_1 chemistry.[1,54] As shown in Fig. 2, the B^{2Pt} site is the most suitable adsorption site for CH_2CO on $Pt_3Sn(111)$ via the $\eta^1(C^\alpha)$-$\eta^1(C^\beta)$ mode, as mirrored by the adsorption energy of 0.73 eV. It is similar to the CH_2CO adsorptions on Pd(111)[50] and Pt(111)[51]. The B^{2Pt}-$\eta^1(C^\alpha)$-$\eta^1(C^\beta)$ configuration is featured by the C^α–Pt and C^β–Pt bond lengths of 2.07 and 2.11 Å, respectively. This adsorption results in the C–C bond elongations from 1.32 to 1.49 Å.

Ketenyl (CHCO). CHCO appears in diversity of reactions as a crucial intermediate, but the spectroscopic information of CHCO is scarce.[55] Our results show that the gas-phase CHCO is a linear radical, in which both C atoms are *sp* hybridized; the C–O, C–C and C–H bond lengths are calculated to be 1.19, 1.29 and 1.08 Å, respectively, in good agreement with the previous results of 1.17, 1.29 and 1.07 Å.[55] Analogous to the Pd(111)[50] and Pt(111)[51] surfaces, CHCO interacts with the $Pt_3Sn(111)$ surface via the $\eta^1(C^\alpha)$-$\eta^2(C^\beta)$ mode at the H^{3Pt} site (see Fig. 2), in which the C^α atom locates at the T^{Pt} site through the sp^2 hybridization ($d_{C\text{-}Pt}$ = 2.10 Å) and C^β at the B^{2Pt} site ($d_{C\text{-}Pt}$ = 2.12 and 2.12 Å) through the sp^3 hybridization. The adsorption energy is 2.53 eV. Other three adsorption configurations for CHCO on $Pt_3Sn(111)$ are B^{2Pt}-$\eta^2(C^\beta)$, F^{2PtSn}-$\eta^1(C^\alpha)$-$\eta^2(C^\beta)$ and F^{3Pt}-$\eta^1(C^\alpha)$-$\eta^2(C^\beta)$ with the energy of 2.20, 1.77 and 1.77 eV, respectively (see Fig. S1).

Carbon Monoxide (CO). CO prefers the T^{Pt} site via the $\eta^1(C)$ mode on the $Pt_3Sn(111)$ surface, in which the C–O axis is almost perpendicular to the surface. The adsorption energy is 1.45 eV, lower than the previous DFT result of 1.82 eV[56] and experimental result of 1.80 eV[57,58] on Pt(111); the C–O bond length is 1.16 Å and the C–Pt bond length is 1.89 Å (see Fig. 2). Comparatively, it is a weak physical absorption for CO at the T^{Sn} site, as reflected by the small adsorption energy of 0.13 eV (see Fig. 2). This indicates that the Sn can weaken the CO adsorption on the Pt slab, and facilitate the elimination of the decomposition product of CO.[30] Besides, CO can adsorb at the B^{2Pt}, B^{PtSn}, F^{3Pt} and H^{3Pt} sites with the C–Pt distances around 2.10 Å (see Fig. S1). The adsorption energies are 1.09 (B^{2Pt}), 1.10 (B^{PtSn}), 0.77 (F^{3Pt}) and 1.27 eV (H^{3Pt}).

H and CH_2. The atomic H can adsorb at the T^{Pt}, F^{3Pt} and H^{3Pt} sites with very close binding energies of 2.70 ~ 2.95 eV, but it is only 1.50 eV at the T^{Sn} site. CH_2 can be stably adsorbed at the B^{2Pt} and B^{PtSn} sites on $Pt_3Sn(111)$ with binding energies of 3.96 and 3.04 eV, respectively. At the B^{2Pt} site, CH_2 forms a tetrahedral adsorption configuration (see Fig. 2), similar to our previous DFT findings on Pd(111);[50] the H–C–H angle is 110° and both C–Pt bond lengths are 2.10 Å. At the B^{PtSn} site (see Fig. S1), the H–C–H angle is 113°, and the C–Pt and C–Sn bond lengths are 2.09 and 2.22 Å, respectively.

3.2 Reaction pathways

In this section, the elementary steps of ethanol decomposition to CO on $Pt_3Sn(111)$ are discussed. To explore the whole reaction network, however, is a tremendous task because ethanol and its decomposition derivatives contain several types of chemical bonds (C–C, C–O, C^α–H, C^β–H and O–H bond). To map it out, we take a recursive "trial-and-error" approach as used in previous work about ethanol decomposition on Rh(111),[1] Pd(111)[50] and Pd(110).[5] Besides, our previous studies found that the initial C–O bond was hardly broken, and it would become more and more difficult along the decomposition route.[5,52] So, in this work, we focus on other types of bond scission. The associated thermodynamic and kinetic parameters are listed in Table 2, and Fig. 3 presents a sketch of the decomposition network. The structures for the IS, TS and FS involved in the elementary steps are shown in Fig. 4.

Decomposition of Ethanol. Four adsorbed ethanol configurations, as the starting point, are considered as ISs due to the close adsorption energy. The initial reaction may involve in ethanol decomposition to CO on the C–C, C^α–H, C^β–H, and O–H bond activation, as shown in Table 2. The O–H bond scission is most favorable for these four ISs as the initial reaction due to the lower energy barriers involved, especially for the T^{Pt}-η^1(O)-*trans* configuration (0.90 eV). Considering the larger ratio of Pt in the alloy, we first check the reaction starting with the T^{Pt}-η^1(O)-*trans* configuration (see Fig. 4a). In this step, approaching of the H atom towards the alloy surface facilitates the O–H activation, as mirrored by the elongated O–H distance to 1.46 Å in the TS1; CH_3CH_2O locates at the same Pt atom as that in the IS ($d_{O\text{-}Pt}$ = 2.23 Å), while the dissociated H moves to the adjacent Pt atom ($d_{H\text{-}Pt}$ = 1.74 Å). After the TS, both dissociated entities diffuse to exact top sites as the FS. This process is endothermic by 0.77 eV and the energy barrier is 0.90 eV. Considering the T^{Sn}-η^1(O)-*trans* configuration is most stable, the initial reaction is also described in detail. In this step, the O–H activation is also beneficial from the approaching of *trans*-ethanol towards the surface (see Fig. S2 (a11)). In the TS, CH_3CH_2O still locates atop the same Sn atom ($d_{O\text{-}Sn}$ = 2.22 Å) while the dissociated H moves to the adjacent off-top site ($d_{H\text{-}Sn}$ = 1.71 Å); the O–H bond is broken as mirrored by its distance of 1.60 Å. After the TS, diffusion of the H entity to the adjacent hcp site accounts for the FS. This process has an energy barrier of 1.12 eV and is endothermic by 0.43 eV. The O–H bond scission of *cis*-ethanol and other bond scission are obviously unfavorable, as reflected by the high energy barriers and low rate constants in Table 2 and Fig. S2 (a1-a15).

Table 2 Thermodynamic and kinetic parameters (in eV and s^{-1}) for the elementary step involved in ethanol decomposition to CO on $Pt_3Sn(111)$.[a]

Reaction / Species	C–C scission			C^{α}–H scission			C^{β}–H scission			O–H scission		
	ΔE	E_a	k	ΔE	E_a	k	ΔE	E_a	k	ΔE	E_a	k
C_2H_5OH-T^{Pt}-*trans*	1.08	3.46	8.61×10^{-44}	0.25	1.53	2.02×10^{-10}	0.61	2.06	4.75×10^{-19}	0.77	0.90	1.65
C_2H_5OH-T^{Pt}-*cis*	0.96	3.76	1.58×10^{-48}	0.24	1.62	2.02×10^{-12}	0.18	1.59	4.64×10^{-12}	0.72	0.98	7.53×10^{-4}
C_2H_5OH-T^{Sn}-*trans*	1.12	3.51	1.58×10^{-43}	0.45	1.24	3.49×10^{-5}	0.47	2.14	2.53×10^{-20}	0.43	1.12	2.97×10^{-4}
C_2H_5OH-T^{Sn}-*cis*	1.17	3.77	3.77×10^{-48}	0.26	1.24	1.53×10^{-5}	0.38	2.26	8.58×10^{-22}	0.57	0.98	4.20×10^{-2}
CH_3CH_2O-T^{Sn}	0.95	2.25	8.27×10^{-23}	-0.56	0.40	4.61×10^{8}	0.32	1.03	8.64×10^{-4}			
CH_3CH_2O-T^{Pt}	0.57	3.02	7.51×10^{-33}	-0.17	0.73	4.13×10^{3}	0.41	1.10	2.64×10^{-3}			
CH_3CH_2O-B^{2Pt}	0.73	3.10	1.43×10^{-33}	0.13	0.98	1.11	0.57	1.28	1.93×10^{-6}			
CH_3CHO-T^{Sn}	0.52	2.09	4.83×10^{-22}	-0.24	0.76	6.78×10^{1}	0.18	1.01	2.86×10^{-2}			
CH_3CO	0.26	2.09	1.95×10^{-20}				0.45	1.64	8.83×10^{-12}			
CH_2CO	1.34	1.57	1.41×10^{-12}				1.36	2.50	3.46×10^{-26}			

[a] Reaction energies of the reactions are calculated as $\Delta E = E_{FS} - E_{IS}$, where E_{FS} and E_{IS} are the energies of the FS and IS, respectively. ΔE and E_a are energies without ZPE corrections, but k is calculated according to eq.2, in which E_a^0 is calculated with ZPE corrections.

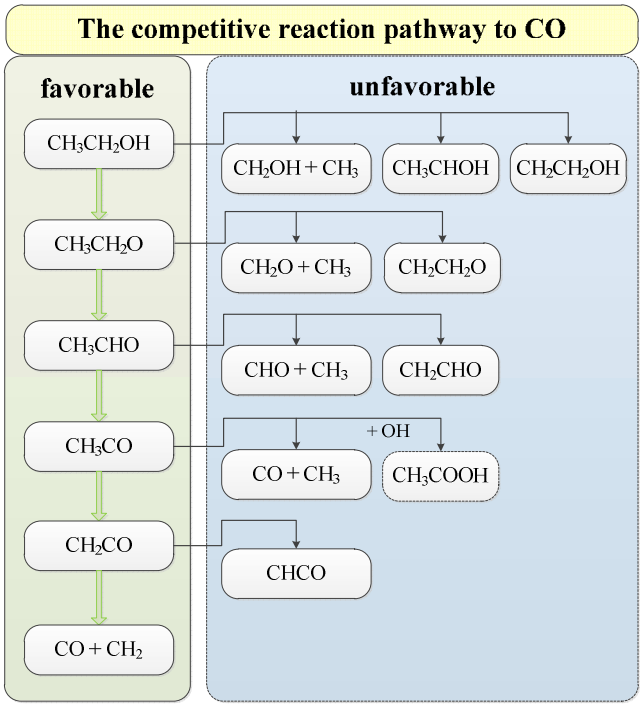

Fig. 3. Reaction network for ethanol decomposition to CO on $Pt_3Sn(111)$; H atoms are omitted for clarity.

Decomposition of Ethoxy. Decomposition of CH_3CH_2O may involve the C–C, C^{α}–H, and C^{β}–H bond activation. As shown in Table 2, the C–C and C^{β}–H bond activation processes can be neglected because both have energy barriers larger than 1.03 eV and their rate constants are less than 2.64×10^{-3} s^{-1}. The lower energy barrier and the larger rate constant indicate that the C^{α}–H bond scission along the $CH_3CH_2O \rightarrow CH_3CHO + H$ reaction is more favorable. This process can start with CH_3CH_2O at the T^{Sn} site as the IS, ends with CH_3CHO at the T^{Sn} site, and with H at the adjacent H^{3Pt} site as the FS (see Fig. 4b). In the TS2, the activated C^{α}–H bond stretches to 1.64 Å. This step is exothermic by 0.56 eV with the energy barrier of 0.4 eV. As shown in Table 2 and Fig. S2, the C^{α}–H bond scission can also start with the CH_3CH_2O at the T^{Pt} site as the IS. This elementary step is exothermic by 0.17 eV with the energy barrier of 0.73 eV. For CH_3CH_2O at B^{2Pt} site, the C^{α}–H bond scission is slightly endothermic by 0.13 eV with the energy barrier of 0.98 eV. In brief, the reaction $CH_3CH_2O \rightarrow CH_3CHO + H$ is

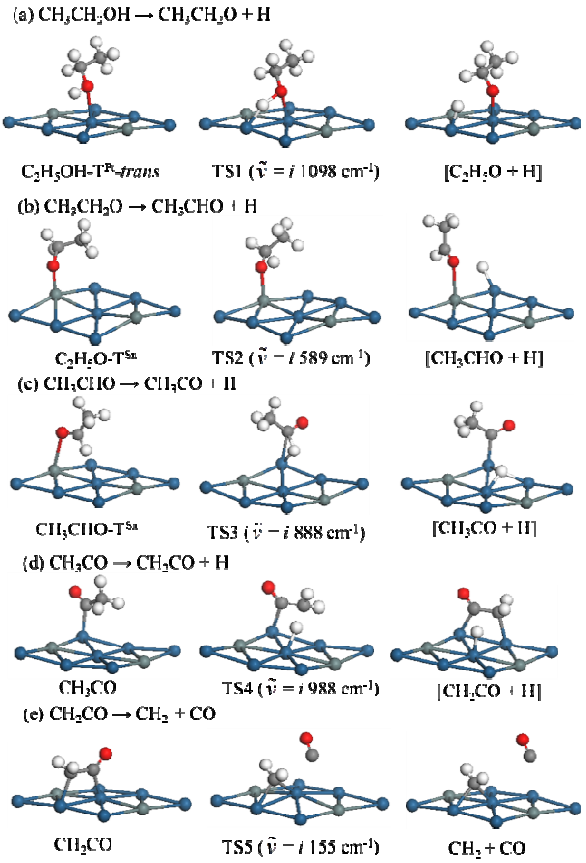

Fig. 4. Calculated structures of the initial state, transition state, and final state involved in the most competitive route of ethanol decomposition to CO on $Pt_3Sn(111)$.

favorable from the viewpoint of thermodynamics and kinetics, especially for the reaction starting with CH_3CH_2O at the T^{Sn} site. Therefore, once CH_3CH_2O is formed, it can quickly decompose to CH_3CHO via C^{α}–H bond scission, thus correlates with the experimental results perfectly that no CH_3CH_2O intermediate is detected for the initial ethanol dehydrogenation on the PtSn alloy.[29,59] Other possible bond scissions of CH_3CH_2O at T^{Pt}, T^{Sn} and B^{2Pt} sites, involving $CH_3CH_2O \rightarrow CH_2CH_2O + H$ and $CH_3CH_2O \rightarrow CH_2O + CH_3$, have high energy barriers and low rate constants as shown in Table 2 and Fig. S2 (b1-b8).

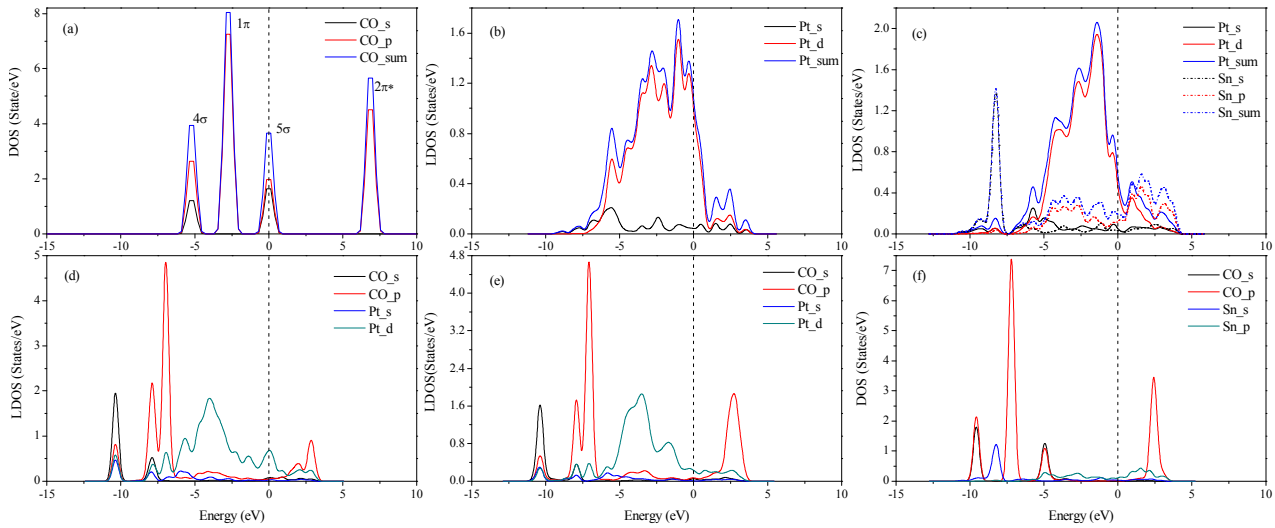

Fig. 5. (a) DOS for gas-phase CO; (b) LDOS of one Pt atom on the first layer of the Pt(111) surface; (c) LDOS of one Pt atom and one Sn atom on the first layer of the $Pt_3Sn(111)$ surface; (d) DOS of adsorbed CO at top site and the involved Pt atom on Pt(111); (e) DOS of adsorbed CO at T^{Pt} site and the involved Pt atom on $Pt_3Sn(111)$; (f) DOS of adsorbed CO at T^{Sn} site and the involved Sn atom on $Pt_3Sn(111)$. Vertical dotted line denotes the Fermi level.

Decomposition of Acetaldehyde. The C–C, C^{α}–H and C^{β}–H bond activation can also be envisaged for further CH_3CHO decomposition. The C^{α}–H bond scission yielding coadsorbed CH_3CO and H is indeed as a favorable process with a low energy barrier of 0.76 eV and a large rate constant of 6.78×10^{1} s^{-1} (see Table 2). This may benefit from the adsorption configuration of CH_3CHO via the η^1(O) mode, and facilitates the C^{α}–H activation. Along the $CH_3CHO \rightarrow CH_3CO + H$ pathway, the stretching vibration of the C^{α}–H bond helps the shift of H from the C^{α} atom of CH_3CHO to the surface Pt atoms. In the TS3 (see Fig. 4c), CH_3CO still locates at the T^{Sn} site as CH_3CHO in the IS, and the dissociated H atom locates at the adjacent B^{2Pt} site with the C^{α}–H distance of 1.43 Å. After the TS3, diffusion of the atomic H to F^{3Pt} site and CH_3CO to T^{Pt} site accounts for the FS. This process is exothermic by 0.24 eV. The C^{β}–H and C–C bond scissions of CH_3CHO, that is, $CH_3CHO \rightarrow CH_2CHO + H$ and $CH_3CHO \rightarrow CHO + CH_3$, have energy barriers of 1.01 and 2.09 eV, and the rate constants of 2.86×10^{-2} s^{-1} and 4.83×10^{-22} s^{-1}, as shown in Table 2 and Fig. S2 (c1-c2).

Decomposition of Acetyl. Two possible bond scissions of the C–C and C^{β}–H bond for the adsorbed CH_3CO are considered. The C^{β}–H bond scission has an energy barrier of 1.64 eV, and its rate constant is about 8 orders larger than that of the C–C bond scission, so the C^{β}–H bond scission to the coadsorbed CH_2CO at the B^{2Pt} site and H at the T^{Pt} site is the favorable decomposition pathway. The C^{β}–H bond scission benefits from the inclined CH_3 in CH_3CO towards the surface so that a methyl H could easily migrate to an adjacent top site. In the TS4, the dissociated H locates at the T^{Pt} site, and CH_2CO still locates at the T^{Pt} site (see Fig. 4d). After the TS, the C–C bond is further inclined to the B^{2Pt} site and the atomic H diffuses to the adjacent T^{Pt} site, forming the FS. The reaction energy of this process is 0.45 eV. Besides, the C–C bond scission of CH_3CO has a high energy barrier of 2.09 eV with the reaction energy of 0.26 eV, and the rate constant of 1.95×10^{-20} s^{-1}, as shown in Table 2 and Fig. S2 (d1).

Decomposition of Ketene. For the adsorbed CH_2CO, as shown in Fig. 4e and Table 2, the favorable decomposition pathway occurs via the C–C bond scission to the coadsorbed CH_2 at the B^{2Pt} site and CO at the T^{Pt} site. This process has the lowest energy barrier of 1.57 eV and the corresponding largest rate constant of 1.41×10^{-12} s^{-1} among all possible C–C bond scissions. In the TS5, both CO and CH_2 locate at the adjacent B^{2Pt} site; the C–C distance is 2.85 Å. After TS5, CO locates at the T^{Pt} site and CH_2 at the adjacent B^{2Pt} site, the C–C distance is elongated to 3.83 Å. This step is highly endothermic by 1.34 eV. The C^{β}–H bond scission of CH_2CO has the largest energy barrier of 2.50 eV and the lowest rate constant of 1.41×10^{-26} s^{-1} among all C^{β}–H bond scissions, as shown in Table 2 and Fig. S2 (e1). To evaluate the effect of surface coverage, we have investigated the CH_2CO decomposition on $Pt_3Sn(111)$ with a large (4 × 4) cell. The relevant structures of each elementary step are shown in Fig. S3. The $CH_2CO \rightarrow CH_2 + CO$ reaction has energy barrier of 1.68 eV and is endothermic by 0.87 eV; For $CH_2CO \rightarrow CHCO + H$, it is endothermic by 1.33 eV with an energy barrier of 2.36 eV. Compared with the results on the (2 × 2) cell, the C–C bond scission of CH_2CO is also favorable than that of C–H bond from both thermodynamic and kinetic viewpoints, and the difference value of energy barrier is 0.11 eV for C–C bond scission and 0.14 eV for C–H bond scission, which is less than 7% in energy barrier and thus indicates the coverage effect is slight on the reaction processes.

4. Discussion

In this section, the intrinsic essence of CO tolerance and the effect of Sn in $Pt_3Sn(111)$ are discussed through adsorption feature and electronic state, reaction mechanism, energy barrier analysis on bond scission, and microkinetic modelling on intermediate coverage.

4.1. Adsorption feature and electronic state

The adsorption configurations of the relevant intermediate, the surface properties of Pt(111) and $Pt_3Sn(111)$, and the electronic states of adsorbed CO on Pt(111) and $Pt_3Sn(111)$ are analyzed in turns. For intermediate adsorption configurations, the most stable configurations are highlighted, i.e., η^1(C) (top) for CH_3CHOH, CH_3CO and CH_3; η^2(C) (bridge) for CH_2; η^1(C)-η^1(O) and η^1(C)-η^1(C) (bridge) for CH_2CH_2O and CH_2CO; η^1(C)-η^2(C) (hollow) for CHCO. These adsorptions are very similar to the species on the

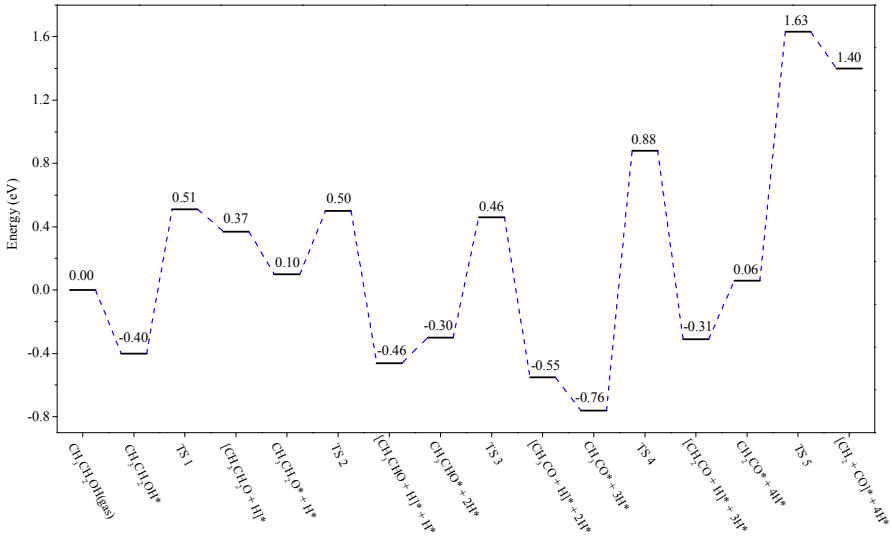

Fig. 6. PES of ethanol decomposition to CO on $Pt_3Sn(111)$. All energies (eV) are relative to the energy of the gas-phase ethanol plus clean $Pt_3Sn(111)$ slab. [A+B]* denotes the coadsorbed A and B, and A*+B* represents respective adsorptions of A and B on two separated slabs.

group VIII metal surfaces, such as Pd(111),[50] reflecting the similarity of the alloy as pure metals to form bonds with the adsorbates. More importantly, these association are strengthened due to the effect of Sn, especially for that via the η^1(O) mode. As seen from Table 1, CH_3CH_2OH, CH_3CH_2O, CH_3CHO and CH_2O at the T^{Sn} site are more stable than those at the T^{Pt} site. That is, Sn plays the "bifunctional" role to strengthen the adsorptions, giving a good support to the experimental result about the Sn effect,[60,61] and similar to the ethylene oxide[62] and cyclohexanone[63] adsorption on PtSn alloys.

To demonstrate the CO tolerance of $Pt_3Sn(111)$, the electronic states of Pt and Sn are investigated by examining the density of states (DOS) of Pt(111) and $Pt_3Sn(111)$. As shown in Fig. 5a, four distinct electron-rich regions appear along the energy scale of the gas-phase CO: 4σ, 1π, 5σ orbitals, and $2\pi^*$ anti-bonding orbitals; the total DOS is mainly composed of the p orbitals, and minor hybridization of p and s orbitals nearby E_F. Fig. 5b presents the local DOS (LDOS) of the Pt atom on the first layer of clean Pt(111) surface, in which the total DOS is mainly composed of the Pt 5d orbitals and minor hybridization of Pt 6s and 5d states nearby -5.60 eV. Fig. 5c shows the LDOS of the Pt and Sn atoms on the first layer of $Pt_3Sn(111)$ surface. For the Pt atom, the total DOS shows similar constituent component to that of the clean Pt(111) except for a more uniform distribution of d states. The LDOS region for the Pt atom nearby E_F decreases sharply, which originates from the hybridization of Pt 5d orbitals with Sn 5p orbitals. This hybridization of Pt 5d orbitals with the electron orbitals of the companion atom nearby E_F is a common bonding mechanism on previous studies of PtSn[64] and similar systems,[65,66] and accounts for the better selectivity of bond scissions on the Pt_3Sn surface.[64] It thus confirms that the Sn atom could effectively adjust the electronic structure of Pt, that is, the "ligand effect" mechanism.

Furthermore, the effect of Sn weakening the Pt–CO bond is evaluated by comparing the DOS of CO on $Pt_3Sn(111)$ with that on clean Pt(111). The LDOS of CO and Pt on Pt(111) is shown in Fig. 5d. Comparing with Figs. 5a and 5b, the adsorption has significant effect on the DOS of CO. All peaks are shifted downward, especially for the peaks of the 5σ and $2\pi^*$ orbitals which decrease to regions at about -4.20 and 2.72 eV. The overlap at -4.20 eV promotes the bonding between CO and Pt atom, originated mainly from the electron donation of the fully occupied CO 5σ orbitals into the Pt 5d orbitals, as well as back-donation of electrons from the Pt 5d orbitals into the unoccupied $2\pi^*$ anti-bonding orbitals at 2.72 eV.[67] This result is close to the adsorption of CO on NiO(100).[68,69] Similar donation and back-donation situation appears for the LDOS of CO at T^{Pt} site and Pt on $Pt_3Sn(111)$, as shown in Fig. 5e. The obvious difference of the adsorbed CO on Pt(111) and $Pt_3Sn(111)$ is the downward-shift value of $2\pi^*$ orbitals, which contributes to the intramolecular bond weakening of CO.[69] The intramolecular bond strength of CO accords well with the geometrical alteration from the gas-phase CO to the adsorbed CO on Pt(111) and $Pt_3Sn(111)$, as reflected by the alteration value of the C–O bond length (0.012 *vs.* 0.015 Å). In addition, the 5σ orbitals (nearby -4.10 eV) of the adsorbed CO on Pt(111) and $Pt_3Sn(111)$ are close, forming a similar Pt–CO bond[69] but with rather weaker adsorption energy of CO on $Pt_3Sn(111)$ (1.82 *vs.*1.45 eV).[56] The LDOS of the adsorbed CO at the T^{Sn} site and Sn on $Pt_3Sn(111)$ is shown in Fig. 5f. Comparing with Fig. 5a, all peaks of CO are shifted downward without any obvious broadening, thus explaining the weakest adsorption mode at the T^{Sn} site with the adsorption energy of 0.13 eV. It means that the adsorption of CO would be weakened, whether it is located at Pt or Sn on Pt_3Sn. That is, the existence of Sn atoms at the $Pt_3Sn(111)$ surface has a positive effect on the CO elimination from the catalyst surface due to the "ligand effect" mechanism.

4.2. Reaction mechanism

The PES for ethanol decomposition to CO along the lowest energy barrier pathway on $Pt_3Sn(111)$ is illustrated in Fig. 6. The energy reference used here corresponds to the total energy of one gas-phase ethanol molecule plus one clean $Pt_3Sn(111)$ slab. In order to elucidate the reaction mechanism clearly, the rate constant is calculated for each elementary step at 300 K, as shown in Table 2. The overall reactions can be described as follows: ethanol adsorbs initially at the T^{Pt} site and then the O–H bond activation to CH_3CH_2O occurs with an energy barrier of 0.90 eV and a rate constant of 1.65 s^{-1}. The following C^{α}–H bond scission of CH_3CH_2O results in CH_3CHO with the lowest barrier of 0.40 eV and the largest rate constant of 4.61×10^8 s^{-1}. The adsorbed CH_3CHO would further dehydrogenate via the C^{α}–H bond activation to CH_3CO with an energy barrier of 0.76 eV and a rate constant of 6.78×10^1 s^{-1}. Next, the C^{β}–H bond activation of CH_3CO accounts for CH_2CO with an

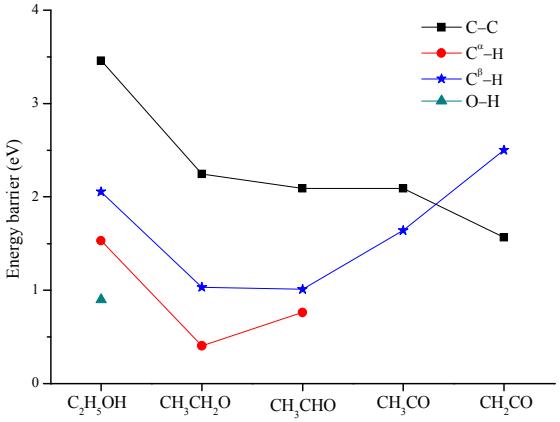

Fig. 7. Energy barrier curves for the C–C, C^{α}–H, C^{β}–H and O–H bond scission in intermediates along the favorable ethanol decomposition pathways on $Pt_3Sn(111)$.

energy barrier of 1.64 eV and a rate constant of 8.83×10^{-12} s^{-1}. The C–C bond activation of CH_2CO leads to CO with a reasonable barrier of 1.57 eV; comparatively, the C^{β}–H bond activation of CH_2CO to CHCO is hindered by a high barrier of 2.50 eV. As for the rate constant, the decomposition of CH_2CO to CO is about 13 orders of magnitude larger than that of CH_2CO to CHCO (see Table 2). On the whole, the most competitive decomposition route to CO is $CH_3CH_2OH \rightarrow CH_3CH_2O \rightarrow CH_3CHO \rightarrow CH_3CO \rightarrow CH_2CO \rightarrow CH_2 + CO$. This pathway agrees well with previous experimental proposal of ethanol decomposition on Pd(111)[70] and $Pt_3Sn(111)$.[30]

Extended group VIII metals, e.g., Pt, Pd, and Rh, have been considered as model systems to understand the mechanism of ethanol decomposition, and found that the activity and selectivity vary depending on the metals and the surface orientation.[71] To better understand the effect of Sn element in $Pt_3Sn(111)$ for ethanol decomposition, we herein compare our work with the previous studies of ethanol decomposition on Pd(111),[50] Rh(111)[1] and Pt(111)[72] in following several points. First, the initial ethanol decomposition on different metal surface is quite different. The initial C^{α}–H bond scission is favorable on Pd(111),[50] while the initial O–H bond scission is easy to take place on Rh(111)[1] and $Pt_3Sn(111)$. This is due to the different adsorption strengths of CH_3CH_2O and CH_3CHOH in the TS on different metal surface[1]: besides, compared with the initial C^{α}–H and O–H bond scissions, the direct two-H decomposition pathway $CH_3CH_2OH \rightarrow CH_3CHO + 2H$ is favorable for ethanol on Pt(111).[72] However, similar coordination of two-H decomposition pathway cannot be found on $Pt_3Sn(111)$. This may result from the weak adsorption of H on Sn at the T^{Sn} site relative to that on Pt at the T^{Pt} site. That is, the Sn in the Pt_3Sn alloy could not play active roles in the initial double C–H bond scissions at the same time. Secondly, as an important intermediate on Pd(111),[50] Pt(111)[72] and $Pt_3Sn(111)$, CH_3CHO is easy to take place by further decomposition to CH_3CO via the C^{α}–H bond scission. This reaction step has the lowest energy barrier of the overall decomposition network on Pd(111)[50] and Pt(111)[72] and the second-lowest one on $Pt_3Sn(111)$, which may originate from the very weak interaction between CH_3CHO and those surfaces. Thirdly, as desired in fuel cells, ethanol and relevant intermediates act as donors to provide electrons consecutively on the catalyst surface, mainly via dehydrogenation and/or oxidation to acid. On Pt(111), the intermediate CH_3CO would rather react with a surface OH group to CH_3COOH than further dehydrogenation to CH_2CO[72]. The same reaction, $CH_3CO + OH \rightarrow CH_3COOH$, is also considered on $Pt_3Sn(111)$, and the results show that it is easy to proceed with the energy barrier as low as 0.38 eV and an exothermic reaction energy as high as 1.09 eV (see Fig. S2 (f1)). From both kinetics and thermodynamics viewpoints, the further CH_3CO reaction via the oxidation of OH is easy to take place, and is in good agreement with electrochemical experiments that CH_3COOH is one of the intermediates for ethanol oxidation on PtSn catalysts.[29,59,73] Even so, CO poisoning is still a serious problem for most catalysts, especially for the pure metals.[22,27,74] Comparatively, on $Pt_3Sn(111)$, the dehydrogenation process $CH_3CO \rightarrow CH_2CO$ is quite difficult since it is high energy barrier of 1.64 eV; moreover, even formed, CH_2CO as the precursor source of CO would rather readily desorb than decompose, as mirrored by the adsorption energy of 0.73 eV relative to the high energy barrier of 1.57 eV. In a word, beneficial from the easy-oxidated CH_3CO, hard-forming but readily-desorbed CH_2CO, the formation of CO is not facile on Pt_3Sn alloy surface.

4.3. Energy barrier analysis on bond activation

Fig. 7 shows the energy barriers of different bond scission processes as a function of intermediate involved in the favourable ethanol decomposition route on $Pt_3Sn(111)$. The general trends are, with the stepwise strip of H atom, the energy barrier for the C–C bond scission decreases gradually, similar to ethanol decomposition on Rh(111).[1] As for the C^{α}–H and C^{β}–H bond scission, they decrease at first and then climb up. Comparatively, the energy barriers for the C^{α}–H bond scission are relatively lower than the corresponding C–C and C^{β}–H bond scission values, especially for the CH_3CH_2O intermediate with the lowest C^{α}–H bond scission barrier.

To provide further insight into the physical origin and uncover the main factors governing the energy barrier of ethanol decomposition to CO, we decompose E_a using the following formula:[75-78]

$$E_a = \Delta E_{sub} + \Delta E_{AB}^{def} + E_{AB}^{IS} + E_{\text{int}}^{TS} - E_A^{TS} - E_B^{TS} \quad (4)$$

where $\Delta E_{sub} = E_{sub}^{TS} - E_{sub}^{IS}$ measures the influence of the structural change of substrate from IS to TS on the activation barrier; ΔE_{AB}^{def} is named as the deformation energy reflecting the effect of the structural deformation of AB on the barrier, and A represents the O-containing species; E_{AB}^{IS} is the binding energy of AB in the IS; E_A^{TS} (E_B^{TS}) is the binding energy of A(B) at the TS geometry without B(A); E_{int}^{TS} is a quantitative measurement of interaction between A and B in the TS. Obviously, the first four terms contribute positively to E_a while they have a reverse effect for the last two factors. These terms are calculated for the elementary steps as shown in Table 3.

For the C–C bond scission, the energy barrier for CH_3CH_2OH, CH_3CH_2O, CH_3CHO and CH_3CO decomposition is relatively higher than that for CH_2CO. This is due to the relatively weak adsorption of CH_3 at the TS geometry (E_B^{TS}) caused by the steric effect, which elevates E_a significantly. On the other hand, the strong adsorption of CH_2 E_B^{TS} (4.33 eV) counteracts the large deformation energy ΔE_{AB}^{def} (4.27 eV) along $CH_2CO \rightarrow CO + CH_2$ reaction step, making it the lowest energy barrier for the C–C bond scission. Even formed, CO tends to escape from the surface due to the low adsorption energy E_A^{TS} of 0.46 eV. Therefore, combining the above mechanism analysis, CO is not facile to form and remain on Pt_3Sn alloy surface along this pathway. For the other possible reaction step to CO, $CH_3CO \rightarrow CO + CH_3$, the relatively high E_a of 2.09 eV results from the high E_{AB}^{IS} of 2.26 eV and low E_B^{TS} of 0.51 eV. The high E_{AB}^{IS} indicates that the precursor of CO tends to decompose rather than desorb due to the relatively low E_a. However, as the above mechanism analysis shown,

Table 3 Energy barriers and contribution factors (in eV) of the elementary reactions considered for ethanol decomposition to CO on $Pt_3Sn(111)$.

Reactions	ΔE_{sub}	ΔE_{AB}^{def}	E_{AB}^{IS}	E_{int}^{TS}	E_{A}^{TS}	E_{B}^{TS}	E_a
$CH_3CH_2OH \rightarrow CH_2OH + CH_3$	0.13	3.40	0.40	0.43	0.55	0.35	3.46
$CH_3CH_2O \rightarrow CH_2O + CH_3$	0.05	1.38	1.81	-0.20	0.25	0.54	2.25
$CH_3CHO \rightarrow CHO + CH_3$	0.23	2.78	0.45	1.16	1.71	0.82	2.09
$CH_3CO \rightarrow CO + CH_3$	0.25	1.29	2.26	0.08	1.28	0.51	2.09
$CH_2CO \rightarrow CO + CH_2$	0.32	4.27	0.73	1.04	0.46	4.33	1.57
$CH_3CH_2OH \rightarrow CH_3CHOH + H$	0.17	3.52	0.40	0.84	0.55	2.85	1.53
$CH_3CH_2O \rightarrow CH_3CHO + H$	0.08	1.02	1.81	0.44	0.35	2.60	0.40
$CH_3CHO \rightarrow CH_3CO + H$	0.36	1.12	0.45	3.39	2.12	2.44	0.76
$CH_3CH_2OH \rightarrow CH_2CH_2OH + H$	0.13	3.24	0.40	1.16	0.40	2.47	2.06
$CH_3CH_2O \rightarrow CH_2CH_2O + H$	0.12	1.96	1.81	0.44	0.82	2.48	1.03
$CH_3CHO \rightarrow CH_2CHO + H$	0.12	4.00	0.45	0.43	1.16	2.83	1.01
$CH_3CO \rightarrow CH_2CO + H$	0.27	2.23	2.26	2.34	2.67	2.79	1.64
$CH_2CO \rightarrow CHCO + H$	0.23	5.51	0.74	0.91	2.50	2.39	2.50
$CH_3CH_2OH \rightarrow CH_3CH_2O + H$	0.21	2.36	0.40	2.19	1.48	2.78	0.90

$CH_3CO \rightarrow CO + CH_3$ is the most unfavorable pathway relative to the oxidation $CH_3CO + OH \rightarrow CH_3COOH$ and the dehydrogenation $CH_3CO \rightarrow CH_2CO + H$ reaction pathways. In short, reactions via the C–C bond scission to CO are not facile on Pt_3Sn alloy surface.

For the C^{α}–H bond scission, the adsorption energy of H in the TS (E_B^{TS}) is in the range of 2.44 ~ 2.85 eV and thus has little effect on the change of the energy barrier. This results from the tiny alterations of adsorption energy for H at different sites (T^{Pt} and B^{2Pt}). The high E_a for CH_3CH_2OH decomposition is mainly caused by the large deformation energy of CH_3CH_2OH (ΔE_{AB}^{def}, 3.52 eV). For CH_3CH_2O, the weak interaction between CH_3CHO and H in the TS (E_{int}^{TS}, 0.44 eV) and the lowest deformation energy (ΔE_{AB}^{def}, 1.02 eV) render the energy barrier E_a to be the minimum (0.40 eV) among the C^{α}–H bond scission processes. In the case of CH_3CHO, E_a is decreased mainly by the large binding energy of CH_3CO in the TS (E_A^{TS}, 2.12 eV), but elevated by the largest interaction between CH_3CO and H (E_{int}^{TS}, 3.39 eV). For the C^{β}–H bond scission, as shown in Table 3, the adsorption energy of atomic H in the TS E_B^{TS} and ΔE_{sub} has relatively slight fluctuation from 2.39 to 2.83 eV and 0.12 to 0.27 eV, respectively, indicating both E_B^{TS} and ΔE_{sub} have little effects on the fluctuation of energy barrier. Comparatively, three positive terms, $\Delta E_{AB}^{def} + E_{AB}^{IS} + E_{\text{int}}^{TS}$, have greater influences on E_a for CH_3CO and CH_2CO decompositions than those for CH_3CH_2OH, CH_3CH_2O and CH_3CHO decompositions via the C^{β}–H bond scission.

For the O–H bond scission, the value of $\Delta E_{AB}^{def} + E_{\text{int}}^{TS}$ is 4.36 eV, and is similar to the values of the C^{α}–H and C^{β}–H bond scission of 4.40 and 4.55 eV, respectively. These small differences (< 0.20 eV) indicate that the intra-ethanol interaction has slight effect on the energy barrier of the initial dehydrogenation. The value of $E_A^{TS} + E_B^{TS}$ decreases in the order of O–H (4.26 eV) > C^{α}–H (3.40 eV) > C^{β}–H (2.87 eV), corresponding to the order of energy barrier O–H < C^{α}–H < C^{β}–H. That is, the binding energy of the cracked fragment in the TS plays a determinant role in the energy barrier of the initial ethanol dehydrogenation on $Pt_3Sn(111)$.

Table 4 Elementary reactions involved in the microkinetic model for decomposition of ethanol on $Pt_3Sn(111)$.[a]

Step	Surface reactions	E_a	A^0
1	$CH_3CH_2OH(g) + * \leftrightarrow CH_3CH_2OH*$	0.39	--
2	$CH_3CH_2OH* + * \leftrightarrow CH_3CH_2O* + H*$	0.90	2.17×10^{15}
3	$CH_3CH_2O* + * \leftrightarrow CH_3CHO* + H*$	0.40	2.42×10^{15}
4	$CH_3CHO* + * \leftrightarrow CH_3CO* + H*$	0.76	3.97×10^{14}
5	$CH_3CO* + * \leftrightarrow CH_2CO* + H*$	1.64	3.14×10^{16}
6	$CH_2CO* + * \leftrightarrow CH_2* + CO*$	1.57	3.35×10^{14}
7	$CH_2* + H* \leftrightarrow CH_3* + *$	1.39	1.91×10^{16}
8	$CH_3* + H* \leftrightarrow CH_4* + *$	0.99	4.26×10^{14}
9	$H* + H* \leftrightarrow H_2* + *$	0.75	1.63×10^{10}
10	$CO* \leftrightarrow CO(g) + *$	1.45	1.00×10^{14}
11	$CH_4* \leftrightarrow CH_4(g) + *$	0.09	1.00×10^{13}
12	$H_2* \leftrightarrow H_2(g) + *$	0.10	1.00×10^{13}

[a] The * stands for a surface site and X* is an adsorbed specie, and E_a is energy barrier and A^0 is pre-exponential.

4.4. Microkinetic modelling on intermediate coverage

To evaluate the residue information of the reaction intermediate, especially for CO, the microkinetic modelling on the crucial 12 elementary reactions is carried out at different reaction temperature, as shown in Table 4. In the microkinetic model, the adsorption and desorption steps are assumed to be in equilibrium. For the other steps, we apply the pseudo-steady-state approximation, that is, the production and consumption rates of the relevant reactant species are assumed to be identical. This microkinetic modelling approach has been successfully applied to similar systems on previous investigations.[36,79] The detailed description of the microkinetic model and the test results with the different partial pressure on the residue information are given in section 2 of the ESI.

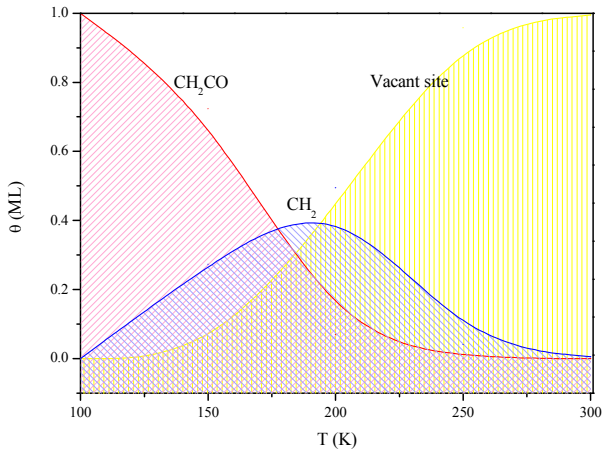

Fig. 8. Surface coverages of CH_2CO, CH_2 and vacant sites as a function of temperature involved in ethanol dehydrogenation on $Pt_3Sn(111)$, and the initial ethanol partial pressure is 1 atm.

The coverage of intermediate (including vacant site) with the value larger than 10^{-2} ML is presented in Fig. 8. The result shows that the CH_2 and CH_2CO intermediates are abundantly detained on the surface, while the CH_3CO and CO intermediates have the largest coverage less than 1.4×10^{-3} ML. This small coverage of CO gives a good support to the experimental result that the Pt_3Sn alloy has the substantially high CO tolerance on ethanol decomposition.[18] For CH_2CO, the largest potential energy of 0.88 eV along $CH_3CH_2OH \rightarrow CH_3CH_2O \rightarrow CH_3CHO \rightarrow CH_3CO \rightarrow CH_2CO$ route is far less than 1.63 eV in the following CH_2CO decomposition, as shown in Fig. 6. Therefore, CH_2CO would be abundantly detained on the surface, as mirrored by the initial value at relatively low temperature in Fig. 8. When temperature increases, the coverage of CH_2CO decreases monotonically. From the microkinetic viewpoint, the elevated temperature would facilitate the decomposition and desorption of CH_2CO. On the other hand, the relatively low coverage of CH_2 at first also reflects the difficult decomposition of CH_2CO at low temperature. Then, with the increase of temperature, the coverage of CH_2 increases and reaches to the top value of almost 0.4 ML at around 180 K, due to the elevated temperature facilitates CH_2CO to CH_2 and the CH_2 adsorb stably on $Pt_3Sn(111)$ (3.96 eV in Table 1). Finally, this value decreases after the top point since the elevated temperature would facilitate the CH_2 hydrogenation ($CH_2 \rightarrow CH_3 \rightarrow CH_4$) and the CH_x ($x = 3 \sim 4$) desorption from the alloy surface. The number of vacant sites is negligible at low temperatures (< 125 K) and increases monotonically with the temperature rising, and finally reaches almost to 1.0 ML. This means that the vast majority of intermediates and products of ethanol decomposition would escape from the $Pt_3Sn(111)$ surface above the room temperature.

5. Conclusions

Our theoretical investigation sheds new light on the CO tolerance of $Pt_3Sn(111)$ and the effect of alloying element Sn along the ethanol decomposition processes, by means of periodic DFT and microkinetic modelling. A number of main points are summarized:

(1) The most competitive reaction route to CO proceeds via $CH_3CH_2OH \rightarrow CH_3CH_2O \rightarrow CH_3CHO \rightarrow CH_3CO \rightarrow CH_2CO \rightarrow CH_2 + CO$. Beneficial from the easily-oxidated CH_3CO, hard-forming but readily-desorbed CH_2CO, the formation of CO is not facile on the $Pt_3Sn(111)$ alloy surface.

(2) Sn plays the "bifunctional" role in the adsorption of the O-end bound species, and takes the "ligand effect" mechanism to effectively adjust the electronic structure of Pt and weakens the Pt–CO bond, and thus facilitating the CO elimination from the $Pt_3Sn(111)$ alloy surface.

(3) Along the favorable route, energy barrier for the C–C bond scission is gradually decreased but still less competitive with respect to that in the C^{α}–H, C^{β}–H, and O–H bond scissions, confirming that the reactions via the C–C bond scission to CO are not facile on $Pt_3Sn(111)$. For the initial ethanol dehydrogenation process, the binding energy of the cracked fragments in the TS plays a determinant role in the energy barrier.

(4) Microkinetic modelling analysis shows that CO residue is rare, and thus confirming the substantially high CO tolerance of the Pt_3Sn alloy surface. For the most abundant surface species of CH_2CO and CH_2, as well as the possible products of ethanol decomposition, they tend to escape from the Pt_3Sn surface above the room temperature.

This theoretical work provides a perspective to understand the effect of alloying elements, by analysing the electronic structure alteration of catalyst, selectivity of adsorption, sequence of bond scission, competition of elementary reaction, thermodynamic and kinetic property, coverage of residue, and thus elucidating the intrinsic essence of tolerance of certain species on alloy catalyst.

Acknowledgements

This work was supported by NSFC (21303266), Shandong Province Special Grant for High-Level Overseas Talents (tshw20120745), Shandong Province Natural Science Foundation (ZR2011EMZ002), Promotive Research Fund for Excellent Young and Middle-aged Scientists of Shandong Province (BS2013CL031), PetroChina Innovation Foundation (2013D-5006-0406), and the Fundamental Research Funds for the Central Universities (13CX05020A and 13CX02025A).

Notes and references

[a] College of Science, China University of Petroleum, Qingdao, Shandong 266580, P. R. China
[b] Department of Physics and Materials Science, City University of Hong Kong, Hong Kong SAR, P. R. China
[c] Key Laboratory for Applied Technology of Sophisticated Analytical Instruments, Shandong Academy of Sciences, Jinan, P. R. China

† Electronic supplementary information (ESI) available: The metastable configurations, reactions involved in the ethanol decomposition routes and the microkinetic modelling, and the coverage effect test.

1 M. Li, W. Y. Guo, R. B. Jiang, L. M. Zhao, X. Q. Lu, H. Y. Zhu, D. L. Fu and H. H. Shan, *J. Phys. Chem. C* 2010, **114**, 21493-21503.
2 W. J. Zhou, W. Z. Li, S. Q. Song, Z. H. Zhou, L. H. Jiang, G. Q. Sun, Q. Xin, K. Poulianitis, S. Kontou and P. Tsiakaras, *J. Power Sources* 2004, **131**, 217-223.
3 C. M. Moore, S. D. Minteer and R. S. Martin, *Lab Chip* 2005, **5**, 218-225.
4 S. C. S. Lai, S. E. F. Kleyn, V. Rosca and M. T. M. Koper, *J. Phys. Chem. C* 2008, **112**, 19080-19087.
5 W. Y. Guo, M. Li, X. Q. Lu, H. Y. Zhu, Y. Li, S. R.Li and L. M. Zhao, *Dalton Trans.* 2013, **42**, 2309-2318.
6 E. Antolini, *J. Power Sources* 2007, **170**, 1-12.
7 H. F. Wang and Z. P. Liu, *J. Am. Chem. Soc.* 2008, **130**, 10996-11004.
8 C. Lamy, S. Rousseau, E. M. Belgsir, C. Coutanceau and J. M. Léger, *Electrochim. Acta* 2004, **49**, 3901-3908.
9 S. Beyhan, C. Coutanceau, J. M. Léger, T. W. Napporn and F. Kadırgan, *Int. J. Hydrogen Energy* 2013, **38**, 6830-6841.
10 Igarashi, H.; Fujino, T.; Zhu, Y. M.; Uchida, H.; Watanabe, M. *Phys. Chem. Chem. Phys.* 2001, **3**, 306-314.

11 M. Götz and H. Wendt, *Electrochim. Acta* 1998, **43**, 3637-3644.
12 F. Alcaide, G. Álvarez, N. Tsiouvaras, M. A. Peña, J. L. G. Fierro and M. V. Martínez-Huerta, *Int. J. Hydrogen Energy* 2011, **36**, 14590-14598.
13 N. R. Elezović, L. M. Gajić-Krstajić, L. M. Vračar and N. V. Krstajić, *Int. J. Hydrogen Energy* 2010, **35**, 12878-12887.
14 Z. F. Liu, G. S. Jackson and B. W. Eichhorn, *Energy Environ. Sci.* 2011, **4**, 1900-1903.
15 S. M. M. Ehteshami, Q. Jia, A. Halder, S. H. Chan and S. Mukerjee, *Electrochim. Acta* 2013, **107**, 155-163.
16 Y. M. Liang, H. M. Zhang, Z. Q. Tian, X. B. Zhu, X. L. Wang and B. L.Yi, *J. Phys. Chem. B* 2006, **110**, 7828-7834.
17 H. T. Kim, J. S. Yoo, H.-I. Joh, H. Kim and S. H. Moon, *Int. J. Hydrogen Energy* 2011, **36**, 1606-1612.
18 Z. Liu, G. S. Jackson and B. W. Eichhorn, *Angew. Chem. Int. Ed.* 2010, **49**, 3173-3176.
19 J. H. Kim, S. M. Choi, S. H. Nam, M. H. Seo, S. H. Choi and W. B. Kim, *Appl. Catal. B: Environ.* 2008, **82**, 89-102.
20 E. Lee, A. Murthy and A. Manthiram *Electrochim. Acta* 2011, **56**, 1611-1618.
21 L. Rao, Y. X. Jiang, B. W. Zhang, Y. R. Cai and S. G. Sun, *Phys. Chem. Chem. Phys.* 2014, **16**, 13662-13671.
22 O. Petrii, *J. Solid State Electrochem.* 2008, **12**, 609-642.
23 C. He, H. R. Kunz and J. M. Fenton, *J. Electrochem. Soc.* 1997, **144**, 970-979.
24 M. Watanabe and S. Motoo, *J. Electroanal. Chem. Interfac.* 1975, **60**, 267-273.
25 M. Watanabe and S. Motoo, *J. Electroanal. Chem. Interfac.* 1980, **111**, 261-268.
26 S. Song and P. Tsiakaras, *Appl. Catal. B: Enviro.* 2006, **63**, 187-193.
27 W. J. Zhou, Z. H Zhou, S. Q. Song, W. Z. Li, G. Q. Sun, P. Tsiakaras and Q. Xin, *Appl. Catal. B: Environ.* 2003, **46**, 273-285.
28 T. Frelink, W. Visscher and J. A. R. van Veen, *Langmuir* 1996, **12**, 3702-3708.
29 F. Vigier, C. Coutanceau, F. Hahn, E. M. Belgsir and C. Lamy, *J. Electroanal. Chem.* 2004, **563**, 81-89.
30 R. Alcala, J. W. Shabaker, G. W. Huber, M. A. Sanchez-Castillo and J. A. Dumesic, *J. Phys. Chem. B* 2004, **109**, 2074-2085.
31 A. Haner, P. Ross and U. Bardi, *Catal. Lett.* 1991, **8**, 1-7.
32 A. E. Aksoylu, M. Madalena, A. Freitas, M. F. R. Pereira and J. L. Figueiredo, *Carbon*, 2001, **39**, 175-185.
33 I. Borbáth, D. Gubán, Z. Pászti, I. Sajó, E. Drotár, J. de la Fuente, T. Herranz, S. Rojas and A. Tompos, *Top. Catal.* 2013, **56**, 1033-1046.
34 S. C. Zignani, V. Baglio, J. J. Linares, G. Monforte, E. R. Gonzalez and A. S. Aricò, *Int. J. Hydrogen Energy* 2013, **38**, 11576-11582.
35 Z. F. Xu and Y. X. Wang, *J. Phys. Chem. C* 2011, **115**, 20565-20571.
36 R. B. Jiang, W. Y. Guo, M. Li, H. Y. Zhu, L. M. Zhao, X. Q. Lu and H. H. Shan, *J. Mol. Catal. A Chem.* 2011, **344**, 99-110.
37 B. Delley, *J. Chem. Phys.* 1990, **92**, 508-517.
38 B. Delley, *J. Phys. Chem.* 1996, **100**, 6107-6110.
39 B. Delley, *J. Chem. Phys.* 2000, **113**, 7756-7764.
40 J. P. Perdew, *Phys. Rev. B* 1986, **33**, 8822-8824.
41 J. P. Perdew and Y. Wang, *Phys. Rev. B* 1992, **45**, 13244-13249.
42 J. P. Perdew, K. Burke and M. Ernzerhof, *Phys. Rev. Lett.* 1996, **77**, 3865-3868.
43 B. Delley, *Phys. Rev. B* 2002, **66**, 155125-155133.
44 H. J. Monkhorst and J. D. Pack, *Phy. Rev. B* 1976, **13**, 5188-5192.
45 M. Hoheisel, S. Speller, J. Kuntze, A. Atrei, U. Bardi and W. Heiland, *Phys. Rev. B* 2001, **63**, 245403.
46 T. A. Halgren and W. N. Lipscomb, *Chem. Phys. Let.* 1977, **49**, 225-232.
47 W. F. K. Wynne-Jones and H. Eyring, *J. Chem. Phys.* 1935, **3**, 492-502.
48 C. Popa, W. K. Offermans, R. A. van Santen and A. P. J. Jansen, *Phys. Rev. B* 2006, **74**, 155428-155437.
49 R. C. Weast, *Am. J. Med. Sci.* 1969, **257**, 423-430.
50 M. Li, W. Y. Guo, R. B. Jiang, L. M. Zhao and H. H. Shan, *Langmuir* 2010, **26**, 1879-1888.
51 R. Alcalá, M. Mavrikakis and J. A. Dumesic, *J. Catal.* 2003, **218**, 178-190.
52 T. Inui and T. Yamamoto, *Catal. Today* 1998, **45**, 209-214.
53 Y. Wang, H. Y. Luo, D. B. Liang and X. H. Bao, *J. Catal.* 2000, **196**, 46-55.
54 K. I. Gursahani, R. Alcala´, R. D. Cortright and J. A. Dumesic, *Appl. Catal. A: Gen.* 2001, **222**, 369-392.
55 P. G. Szalay, G. Fogarasi and L. Nemes, *Chem. Phys. Lett.* 1996, **263**, 91-99.
56 J. Greeley and M. Mavrikakis, *J. Am. Chem. Soc.* 2004, **126**, 3910-3919.
57 Y. Y. Yeo, L. Vattuone and D. A. King, *J. Chem. Phys.* 1997, **106**, 392-401.
58 D. C. Ford, Y. Xu and M. Mavrikakis, *Surf. Sci.* 2005, **587**, 159-174.
59 H. Wang, Z. Jusys and R. J. Behm, *J. Power Sources* 2006, **154**, 351-359.
60 W. J. Zhou, S. Q. Song, W. Z. Li, Z. H. Zhou, G. Q. Sun, Q. Xin, S. Douvartzides and P. Tsiakaras, *J. Power Sources* 2005, **140**, 50-58.
61 M. H. M. T. Assumpção, J. Nandenha, G. S. Buzzo, J. C. M. Silva, E. V. Spinacé, A. O. Neto and R. F. B. De Souza, *J. Power Sources* 2014, **253**, 392-396.
62 J. Kim, J. Fu, S. G. Podkolzin and B. E. Koel, *J. Phys. Chem. C*, 2010, **114**, 17238-17247.
63 J. Kim, L. A. Welch, A. Olivas, S. G. Podkolzin and B. E. Koel, *Langmuir* 2010, **26**, 16401-16411.
64 Pick, Š. *Surf. Sci.* 1999, **436**, 220-226.
65 Pick, S. *J. Phy. Condens. Matter* 1997, **9**, 141-148.
66 M. Weinert and R. E. Watson, *Phys. Rev. B* 1995, **51**, 17168-17180.
67 S. E. Mason, I. Grinberg and A. M. Rappe, *J. Phys. Chem. C* 2008, **112**, 1963-1966.
68 G. Pacchioni, G. Cogliandro and P. S. Bagus, *Surf. Sci.* 1991, **255**, 344-354.
69 A. Rohrbach, J. Hafner and G. Kresse, *Phys. Rev. B* 2004, **69**, 075413.
70 M. Mavrikakis and M. A. Barteau, *J. Mol. Catal. A: Chem.* 1998, **131**, 135-147.
71 P. Liu, Y.X. Yang and M. G. White, Surf. Sci. Rep., 2013, **68**, 233-272.
72 H. F. Wang and Z. P. Liu, *J. Phys. Chem. C* 2007, **111**, 12157-12160.
73 F. Vigier, C. Coutanceau, A. Perrard, E. M. Belgsir and C. Lamy, *J. Appl. Electrochem.* 2004, **34**, 439-446.
74 J. Friedl and U. Stimming, *Electrochim. Acta* 2013, **101**, 41-58.
75 Y. Cao and Z. X. Chen, *Phys. Chem. Chem. Phys.* 2007, **9**, 739-746.
76 X. Q. Lu, Z. G. Deng, K. S. Chau, L. F. Li, Z. Q. Wen, W. Y. Guo and C. M. L. Wu, *ChemCatChem* 2013, **5**, 1832-1841.
77 Z. G. Deng, X. Q. Lu, Z. Q. Wen, S. X. Wei, Y. J. Liu, D. L. Fu, L. M. Zhao and W. Y. Guo, *Phys. Chem. Chem. Phys.* 2013, **15**, 16172-16182.
78 Z. G. Deng, X. Q. Lu, Z. Q. Wen, S. X. Wei, Q. Zhu, D. L. Jin, X. F. Shi and W. Y. Guo, *RSC Adv.*, 2014, **4**, 12266-12274.
79 Y. Choi and P. Liu, *J. Am. Chem. Soc.* 2009, **131**, 13054-13061